Mesoscale Temperature Fluctuations Induced by a Spectrum of Gravity Waves: A Comparison of Parameterizations and Their Impact on Stratospheric Microphysics

JULIO T. BACMEISTER

Universities Space Research Association, Columbia, Maryland

STEPHEN D. ECKERMANN

Computational Physics, Inc., Fairfax, Virginia

ATHANASIOS TSIAS, KENNETH S. CARSLAW, AND THOMAS PETER

Max Planck Institute for Chemistry, Mainz, Germany

(Manuscript received 20 January 1998, in final form 27 July 1998)

ABSTRACT

Power spectral densities (PSDs) of mesoscale fluctuations of temperature and rate of change of temperature (heating–cooling rate) due to a spectrum of stratospheric gravity waves are derived using canonical spectral forms based on observations and linear gravity wave theory. The parameterization developed here assumes a continuous distribution of horizontal wave phase speeds, as opposed to a previous spectral parameterization in which all waves were assigned stationary ground-based phase speeds. Significantly different heating–cooling rate PSDs result in each case. The differences are largest at small horizontal scales, where the continuous phase-speed parameterization yields heating–cooling rate PSDs that are several orders of magnitude smaller than in the stationary phase-speed parameterization. A simple Monte Carlo method is used to synthesize randomly phased temperature perturbation time series within tagged air parcels using either spectral parameterization. These time series are incorporated into a nonequilibrium, microphysical trajectory-box model to assess the microphysical consequences of each parameterization. Collated results yield a ''natural'' geophysical scatter of instantaneous aerosol volumes within air parcels away from equilibrium conditions. The amount of scatter was much smaller when the continuous phase-speed parameterization was used.

1. Introduction

The importance of polar stratospheric clouds (PSCs) in ozone depletion has prompted considerable research into their composition and formation. Observations show that PSCs often form preferentially over mountainous terrain, where they seem to be associated with the penetration of mountain lee waves into the stratosphere (e.g., Cariolle et al. 1989; Deshler et al. 1994; Godin et al. 1994; Fromm et al. 1997; Carslaw et al. 1998a,b). Recent modeling work has shown that mountain wave temperature perturbations affect the formation and growth of aerosol particles, as well as subsequent heterogeneous chemical reactions that take place on the particles (e.g., Peter et al. 1994; Meilinger et al. 1995; Borrmann et al. 1997; Tsias et al. 1997). This occurs because microphysical processes have a strongly nonlinear dependence on both temperature (e.g., Tabazadeh et al. 1994; Carslaw et al. 1994) and the rate of change of temperature (e.g., Meilinger et al. 1995; Tsias et al. 1997). Thus, details in air parcel temperature histories can have an important impact on microphysical end products, such as particle size distributions, total aerosol volume, and particle freezing (Drdla and Turco 1991; Jensen and Toon, 1994; Koop et al. 1995, 1997; Tsias et al. 1997). Furthermore, several important heterogeneous reaction rates have a strong temperature dependence (e.g., Borrmann et al. 1997), which leads to rates of chlorine activation in stratospheric mountain waves that are orders of magnitude faster than those encountered synoptically (Carslaw et al. 1998a). Carslaw et al. (1998b) have proposed that the combined effect of all such mountain waves in the Arctic could cause an overall decrease in ozone levels. The temperature oscillations of a gravity wave have also been shown to be important in microphysical models of polar mesospheric clouds (Turco et al. 1982; Jensen and Thomas 1994)

Corresponding author address: S. D. Eckermann, E. O. Hulburt Center for Space Research, Code 7641, Naval Research Laboratory, Washington, DC 20375.
E-mail: eckerman@uap.nrl.navy.mil

and of high cirrus clouds (Potter and Holton 1995; Jensen et al. 1996; Lin et al. 1998).

All of these model studies considered the microphysical effects of single waves, whereas observations reveal that, on average, broad pseudorandom spectra of temperature fluctuations exist in the stratosphere (e.g., Nastrom and Gage 1985; Tsuda et al. 1991; Bacmeister et al. 1996; Whiteway et al. 1997). Tabazadeh et al. (1996) parameterized this by assuming Gaussian probability density functions (PDFs) of mesoscale temperature fluctuations due to a spectrum of waves, basing their variances on stratospheric data taken from the microwave temperature profiler (MTP) on the National Aeronautics and Space Administration's (NASA) ER-2 research aircraft. Murphy and Gary (1995, hereafter MG95) also addressed this issue by deriving mesoscale horizontal wavenumber spectra of temperature, heating–cooling rate (i.e., rate of change of temperature, negative if cooling), and PSC supersaturation fluctuations, based on the temperature spectra observed from MTP and other in situ aircraft measurements in the lower stratosphere.

The calculations of MG95 were based on the implicit assumption that mesoscale temperature fluctuations observed by the aircraft were stationary with respect to the ground, implying a spectrum of gravity waves with stationary ground-based horizontal phase speeds (such as mountain waves). However, analysis of accumulated meteorological measurement system (MMS) data from stratospheric ER-2 flights led Bacmeister et al. (1996, hereafter B96) to different conclusions. They compared fluctuations in these data with idealized models of the two-dimensional (2D) spectrum of gravity wave–induced horizontal velocities as a function of vertical wavenumber m, and intrinsic frequency ω, $G_{u,v}(m, \omega)$. This continuous 2D spectrum implies a broad, continuous distribution of wave phase speeds, in contrast to the MG95 model. B96 used linear gravity wave theory to transform $G_{u,v}(m, \omega)$ into corresponding spectral predictions for the one-dimensional horizontal wavenumber (k) spectra of horizontal velocities $F_{u,v}(k)$ and vertical velocities $F_w(k)$ (Gardner et al. 1993a,b). Excellent agreement was found between these theoretical spectra and corresponding spectra derived from MMS data, leading them to conclude that mesoscale temperature and velocity fluctuations in stratospheric ER-2 data were consistent with a spectrum of gravity waves with a broad distribution of horizontal phase speeds.

In this paper, we go on to develop a spectral parameterization of mesoscale temperature and heating rate perturbations based on the continuous phase-speed model of Gardner et al. (1993a,b) and B96, and compare it with the stationary phase-speed parameterization of MG95. We demonstrate that, in each case, very different temperature and heating–cooling rate perturbations arise within air parcels as they are advected through the wave fields. Reanalysis of MMS data reveals that PDFs of mesoscale temperature amplitudes in the stratosphere are approximately Gaussian, with departures only in the ''wings'' of the distribution. We associate the Gaussian components of the PDFs with the basic background spectrum of wave activity that is always present in the stratosphere, and the non-Gaussian tails with intermittent large-amplitude wave events. We go on to generate synthetic time series of parcel-based temperature perturbations using a simple Monte Carlo method, which yields Gaussian temperature PDFs that can be governed by either the MG95 or B96-based spectral parameterizations. Finally, we use these artificial time series within a microphysical box-trajectory model for the stratosphere to assess the microphysical impacts of each parameterization.

2. Spectral parameterization

In their analysis of velocity and temperature fluctuation spectra from MMS data from the lower stratosphere, B96 used linear polarization and dispersion relations for hydrostatic, nonrotating gravity waves to transform models for the 2D gravity wave spectrum $G_{u,v}(m, \omega)$ into corresponding predictions for the one-dimensional horizontal wavenumber spectra of horizontal velocities $F_{u,v}(k)$ and vertical velocities $F_w(k)$ that are measured by the aircraft (Gardner et al. 1993a,b). A further assumption of horizontal isotropy in wave propagation directions was made in these theoretical derivations. B96 found excellent agreement between the velocity spectra observed by MMS and theoretical predictions for $F_{u,v}(k)$ and $F_w(k)$ based on a separable analytical hydrostatic gravity wave spectral model of the form

$$G_{u,v}(m, \omega) = E_0 \hat{A}_{u,v}(m) \hat{B}_{u,v}(\omega), \tag{1}$$

where $\hat{A}_{u,v}(m)$ and $\hat{B}_{u,v}(\omega)$ are normalized 1D model spectra and E_0 is the total wave energy per unit mass (Fritts and VanZandt 1993). The shapes of the 1D model spectra are discussed in depth by Gardner et al. (1993a,b), Fritts and VanZandt (1993), and B96. Briefly, the vertical wavenumber spectrum $\hat{A}_{u,v}(m) \rightarrow m^{-3}$ at large m and peaks at a characteristic wavenumber m_*, which is around 2π (2–3 km)$^{-1}$ in the lower stratosphere. The normalized frequency spectrum takes the form $\hat{B}_{u,v}(\omega) \propto [1 + (f/\omega)^2]\omega^{-p}$ between the allowed intrinsic frequencies $|f| < |\omega| < N$ [$\hat{B}_{u,v}(\omega) = 0$ elsewhere], where f is the Coriolis parameter, N is the background Brunt–Väisälä frequency, and $p = 2$. These shapes are based on both theory and accumulated data, and although nonseparable models for $G_{u,v}(m, \omega)$ have also been proposed (e.g., Gardner 1996; Dewan 1997), the separable form, (1), is still used commonly in the stratosphere (e.g., Gardner et al. 1993a,b; Fritts and VanZandt 1993). The model (1) implies a broad continuous distribution of wave phase speeds within the spectrum, as opposed to the stationary phase-speed model of MG95.

We now apply the model (1) to predict PSDs of temperature and heating–cooling rate perturbations.

a. Temperature PSDs

B96 also evaluated PSDs of MMS potential temperature data and compared them to the predictions of the model (1). Simple polarization relations for hydrostatic gravity waves lead to the relation

$$G_T(m,\,\omega) = \left(\frac{\overline{T}}{\overline{\Theta}}\right)^2 G_\Theta(m,\,\omega) = Q(\omega)\left(\frac{N\overline{T}}{g}\right)^2 G_{u,v}(m,\,\omega), \tag{2}$$

where $G_T(m,\,\omega)$ is the 2D gravity wave temperature spectrum; $G_\Theta(m,\,\omega)$ is the potential temperature spectrum; g is gravitational acceleration; $\overline{\Theta}$ and $\overline{T}$ are background potential and absolute temperatures, respectively; and $Q(\omega)$ is the ratio of potential to kinetic energy of a given wave of intrinsic frequency, ω. For hydrostatic waves, $Q(\omega) = 1$ for nonrotating flow and $Q(\omega) = (\omega^2 - f^2)/(\omega^2 + f^2)$ for rotating flow (for the calculations in this paper, we have assumed a nonrotating atmosphere). This leads to model horizontal wavenumber PSDs

$$F_T(k) = T_0^2\hat{F}_T(k) \propto F_\Theta(k) \propto \left(\frac{N\overline{T}}{g}\right)^2 F_{u,v}(k), \tag{3}$$

where T_0^2 is the total temperature variance and $\hat{F}_T(k)$ is the normalized model spectrum. Thus, the potential temperature, absolute temperature, and horizontal velocity fluctuations should all have similarly shaped horizontal wavenumber spectra. B96 showed that $F_\Theta(k)$ and $F_{u,v}(k)$ computed from MMS data had similar shapes and thus agreed well with the model prediction (3) based on (1).

Of additional relevance to microphysics is the intrinsic frequency PSD of temperatures, which governs the time variations of temperature fluctuations within tagged air parcels as they are advected by the background flow. This spectrum is difficult to measure directly. However, it is easily derived from the model spectra (1) and (2), to yield

$$B_T(\omega) = T_0^2\hat{B}_T(\omega) = Q(\omega)\left(\frac{N\overline{T}}{g}\right)^2 E_0\hat{B}_{u,v}(\omega) \equiv B_T^{B96}(\omega), \tag{4}$$

where $\hat{B}_T(\omega)$ is the normalized temperature spectrum.

The present analysis can be contrasted to that of MG95, which assumed (implicitly) that all the waves in the spectrum were stationary with respect to the ground. MG95 used a model for the horizontal wavenumber temperature PSD based on data from various airborne platforms, which exhibited similar spectral shapes to the model spectrum $F_T(k)$ in (3). Under their stationary phase-speed assumption, a Taylor transformation from the ground-based frame to the intrinsic frame[1] yields the intrinsic (parcel based) frequency PSD

$$B_T^{MG95}(\omega,\,\mathcal{U}) = T_0^2\frac{\hat{F}_T(\omega/\mathcal{U})}{\mathcal{U}}, \tag{5}$$

where $\mathcal{U} = (\overline{U}^2 + \overline{V}^2)^{1/2}$ is the background wind speed and $\omega = k\mathcal{U}$. This derivation also assumes no directional variability in $\hat{F}_T(k)$ (i.e., azimuthal isotropy). Note the strong dependence of this parcel-based spectrum on the background wind speed.

b. Heating–cooling rate PSDs

If the wave spectrum is nondissipating, as is often the case in the lower stratosphere [see, e.g., Figs. 7 and 8 of Tsuda et al. (1991)], an air parcel will be displaced adiabatically about its equilibrium position by the wave field. Thus, the potential temperature of the parcel will be conserved, which, for a single wave, yields the linearized perturbation equation

$$D_t\theta' = \partial_t\theta' + \overline{U}\partial_x\theta' + \overline{V}\partial_y\theta' = -\omega'\partial_z\overline{\Theta}, \tag{6}$$

where θ' and ω' are wave-induced perturbations of potential temperature and vertical velocity, respectively; $\overline{U}$ and $\overline{V}$ are the background zonal and meridional winds, respectively; $\overline{\Theta}$ is the background potential temperature; subscripted ∂ terms denote local partial derivatives (i.e., $\partial_t = \partial/\partial t$); and D_t is the intrinsic (parcel based) time derivative. Horizontal gradients in background quantities were neglected in deriving (6).

Hydrostatic gravity waves have shallow vertical structure, and so the temperature and potential temperature perturbations are approximately related, as in (2), according to

$$\frac{\theta'}{\overline{\Theta}} = \frac{T'}{\overline{T}} \tag{7}$$

(e.g., Eckermann et al. 1998). Thus, rearranging terms in (6) and scaling with (7), we obtain the expression

[1] The Taylor transformation converts stationary horizontal wavelength structures in one frame (in this case, the ground-based frame) into temporal variations measured within another frame that is being advected through this horizontal variability (in this case, the intrinsic frame). Note that this is the inverse Taylor transformation to the one used to derive ground-based frequency spectra due to stratified two-dimensional turbulence models, in which the horizontal variability is assumed to be stationary (''frozen'') in the intrinsic frame [see, e.g., Eq. (9) of Vincent and Eckermann (1990)].

$$D_t T = \partial_t T' + \overline{U}\partial_x T' + \overline{V}\partial_y T' = -w'\partial_z \overline{\Theta}\left(\frac{\overline{T}}{\overline{\Theta}}\right)$$

$$= -\left(\frac{\overline{T}N^2}{g}\right)w', \quad (8)$$

for the Lagrangian rate of change of temperature perturbation (i.e., the heating–cooling rate perturbation within an air parcel advected by the mean wind). Thus, for linear adiabatic gravity waves, the heating–cooling rate perturbations are proportional to the vertical velocity perturbations, and so the heating–cooling rate PSD $F_{D_tT}(k)$ follows from simple scaling of the PSD of vertical velocity according to (8):

$$F_{D_tT}(k) = \left(\frac{\overline{T}N^2}{g}\right)^2 F_w(k) \equiv F_{D_tT}^{B96}(k). \quad (9)$$

The horizontal wavenumber PSD of heating–cooling rate fluctuations under the continuous phase-speed model (9) may be contrasted with the one arising from the MG95 stationary phase-speed model, which is given by

$$F_{D_tT}^{MG95}(k, \mathcal{U}) = \mathcal{U}^2 k^2 F_T(k). \quad (10)$$

This relation follows via a Taylor transformation from the ground-based frame (where ∂_t terms vanish since waves are taken to be stationary) to the intrinsic frame to derive the parcel-based time derivative D_t (Murphy and Gary 1995). Note that, unlike (9), the MG95 heating–cooling rate PSD (10) is a strong function of the background wind speed $\mathcal{U}$.

Intrinsic frequency PSDs of heating–cooling rate follow from the corresponding temperature PSDs. For the B96-based model,

$$B_{D_tT}^{B96}(\omega) = \omega^2 B_T^{B96}(\omega), \quad (11)$$

and so is approximately flat given the approximately ω^{-2} shape of $B_T^{B96}(\omega)$ implied by (4). The corresponding PSD from the MG95 model is

$$B_{D_tT}^{MG95}(\omega, \mathcal{U}) = \omega^2 B_T^{MG95}(\omega, \mathcal{U}) = \frac{\omega^2}{\mathcal{U}} F_T(\omega/\mathcal{U}), \quad (12)$$

where $\omega = k\mathcal{U}$.

3. Comparisons with data

To compare the various parameterizations with data, we use vertical velocity and temperature fluctuations derived from MMS data during three aircraft campaigns employing NASA's ER-2 aircraft: 1) the second Arctic Airborne Stratospheric Expedition (AASEII), (2) the Stratospheric Photochemistry Aerosol and Dynamics Experiment (SPADE), and (3) the Airborne Southern Hemisphere Ozone Experiment/Measurements for Assessing the Effects of Stratospheric Aircraft (ASHOE/MAESA) campaign. Locations and dates of these campaigns, as well as a brief description of the MMS dataset, can be found in B96 and references therein. The PSDs used in this study are calculated from discrete wavelet transforms (DWTs) in the manner outlined in B96.

a. Heating–cooling rates PSDs

It was noted in section 2 that the two parameterizations use a similar observationally constrained model for the horizontal wavenumber spectrum of temperatures $F_T(k)$ but derive different heating–cooling rate PSDs from it. These differences are illustrated in Fig. 1. The solid curve with triangular symbols in Fig. 1a shows $F_{D_tT}^{B96}(k)$ derived from MMS vertical velocity spectra using (9). It represents a log average over all flights in the AASEII, SPADE, and ASHOE/MAESA campaigns. The remaining curves in Fig. 1a show $F_{D_tT}^{MG95}(k, \mathcal{U})$ for three $\mathcal{U}$ values of 1, 20, and 50 m s^{-1}, as obtained by scaling a corresponding log-averaged PSD of MMS temperature (shown in Fig. 1b) using (10).

The shapes of the two heating–cooling rate PSDs are clearly very different. The MG95 PSDs are much flatter at small scales. At scales smaller than 6.4 km, $F_{D_tT}^{MG95}(k, \mathcal{U})$ decays weakly with a spectral index between 0 and -1, while $F_{D_tT}^{B96}(k)$ decays more rapidly with a spectral index close to -3. The magnitude of $F_{D_tT}^{MG95}(k, \mathcal{U})$ also depends sensitively on the background flow speed $\mathcal{U}$, since it determines how rapidly the parcels are advected through, and perturbed by, the stationary horizontal wave structures. In contrast, the heating–cooling rate PSD determined from the B96-based parameterization (9) has no explicit dependence on background flow conditions. Observationally, B96 found a weak dependence of the MMS vertical velocity PSD on the magnitude of the background horizontal wind, and other studies have also reported some sensitivities of stratospheric velocity spectra to the background wind profile (e.g., Eckermann 1995). The sensitivity of the MMS vertical velocity PSDs to background wind speed appeared to vary with horizontal scale: at $k > m_*$ the vertical velocity PSDs appeared to be less sensitive to changes in the background wind speed than the PSDs at $k < m_*$ (Bacmeister et al. 1996). So, while some evidence for a dependence on wind speed exists, existing data indicate that it is significantly weaker than the quadratic dependence of $F_{D_tT}^{MG95}(k, \mathcal{U})$ on $\mathcal{U}$ in (10) and Fig. 1a.

Table 1 gives spectrally integrated root-mean-square (rms) heating rates for the B96-based heating–cooling rate spectrum within several logarithmically spaced wavenumber ranges, as determined by numerically integrating $F_{D_tT}^{B96}(k)$ in Fig. 1a. Integrated heating–cooling rates based on (9) peak at scales between ~3 and 25 km. This is in contrast to the MG95 spectral model, which yields integrated heating–cooling rates that increase monotonically as horizontal scales decrease (see Table 1 of MG95).

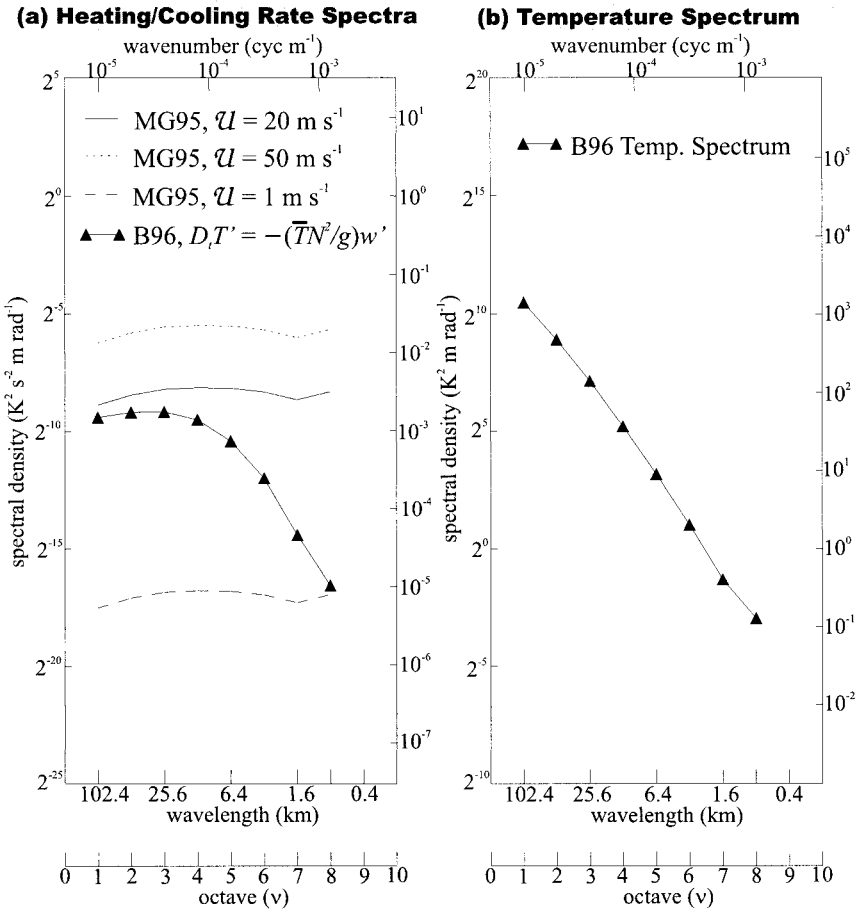

FIG. 1. (a) Power spectral density (PSD) of heating–cooling rate as a function of horizontal wavenumber k; (b) PSD of temperature as a function of k. (a), (b) PSDs are obtained from log averages over all flights in AASE II, SPADE, and ASHOE/MAESA. (a) Filled triangles show heating–cooling rates obtained by scaling the mean PSD of vertical velocity as shown in (3). (b) Solid, dotted, and dashed lines show heating–cooling rates obtained from the horizontal derivative of the mean temperature, following MG95. Results shown are for 3 different values of mean $\mathcal{U}$: 20, 50, and 1 m s^{-1}.

b. Temperature PDFs

Another approach to parameterizing multiwave temperature perturbations within microphysical models is to employ Gaussian PDFs (Tabazadeh et al. 1996). The DWT analysis of MMS data by B96 preserves information about the location and amplitude of fluctuations at each of the characteristic scales (or ''octaves'') resolved by the DWT, which allows us to study temperature fluctuation statistics and PDFs as a function of horizontal scale.

TABLE 1. Rms heating–cooling rates within logarithmically spaced horizontal-scale ranges, using the B96-based model.

Horizontal-scale range (km)	Heating–cooling rate (K day^{-1})
102.4–25.6	±52
51.2–12.8	±71
25.6–6.4	±86
12.8–3.2	±87
6.4–1.6	±70
3.2–0.8	±47

Figure 2 shows PDFs of DWT temperature amplitudes at different horizontal scales. Least squares fits to a Gaussian distribution over the central 68% of the data are also shown. Within $\pm 1\sigma$ of the peak, the PDFs closely approximate a Gaussian distribution, as assumed by Tabazadeh et al. (1996). The rms amplitudes of the fluctuations in Fig. 2 are comparable to those obtained by MG95 at similar horizontal scales.

However, there is evidence of non-Gaussian high-amplitude tails in all of the PDFs in Fig. 2. In other words, high-amplitude temperature fluctuations are somewhat more probable than would be inferred from the Gaussian distributions determined from fits to the central 68% of the data. These departures from Gaussianity become more pronounced as the horizontal scale of the fluctuations decreases in Fig. 2. Chi-squared tests

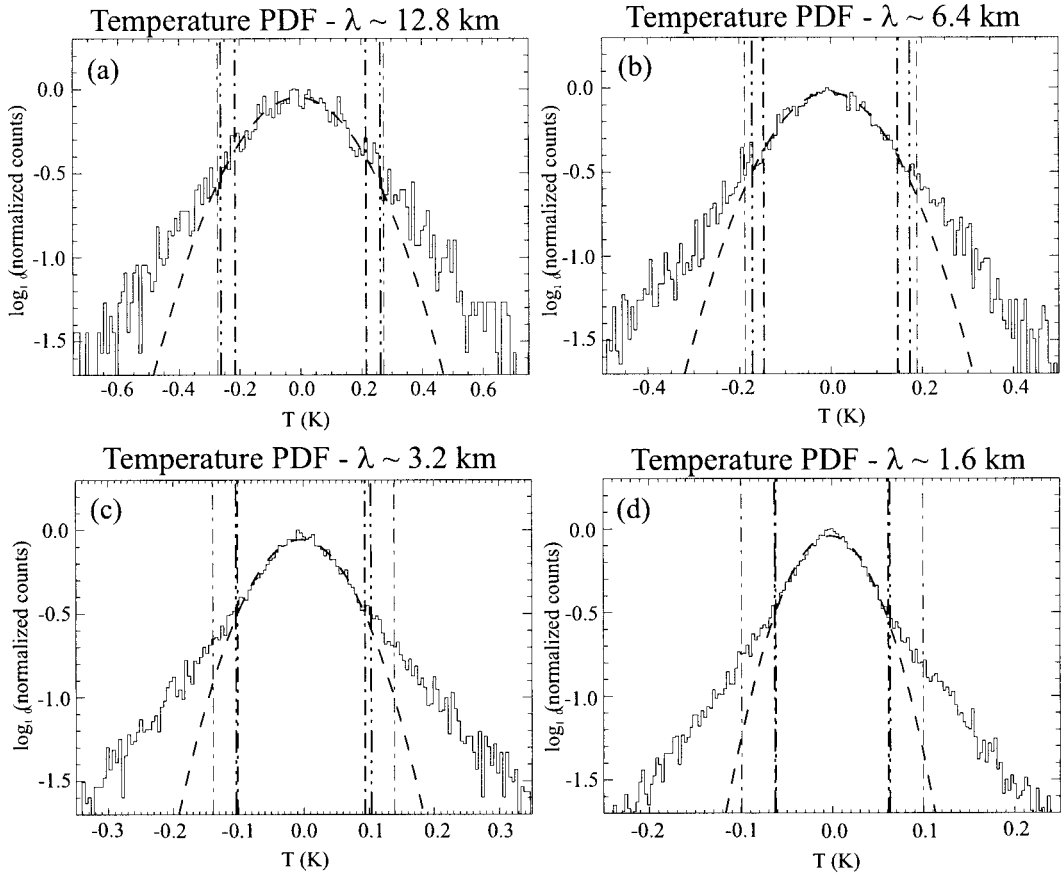

FIG. 2. Log_{10} of normalized PDFs of temperature fluctuation amplitude determined using discrete wavelet transforms of MMS temperatures measured during ASHOE/MAESA. Thick dashed curves show Gaussian fits (which appear parabolic here) to the central 68% of data. Results are shown for fluctuations with characteristic horizontal scales of (a) 12.8, (b) 6.4, (c) 3.2, and (d) 1.6 km. Fluctuation amplitudes appear to be well described by a normal distribution in the central or small-amplitude portion of the distribution. However, PDFs show non-Gaussian, high-amplitude tails, especially at smaller horizontal scales. These may be associated with infrequent high-amplitude wave events, such as waves generated by intense convection or flow over mountains.

of the observed PDFs versus the Gaussian fits indicate that the non-Gaussian behavior in the wings of the distributions is highly significant statistically. Similar behavior is observed in the PDFs of horizontal velocity fluctuations measured by MMS in the stratosphere (Bacmeister et al. 1997a). The origin of the non-Gaussian tails in the temperature fluctuations is not entirely clear. However, intermittent large-amplitude wave events are likely to be at least partially responsible (Bacmeister et al. 1990; Alexander and Pfister 1995).

4. Parameterizations for parcel-based calculations

The spectral parameterizations (3), (9), (10), and those of MG95 are presented as horizontal wavenumber spectra, which govern the horizontal ''line'' distribution of a collection of parcels at a given instant in time. However, many microphysical models are Lagrangian, concentrating instead on time variations of meteorological and microphysical parameters within tagged air parcels as they are advected by the background flow.

For such models, spectral parameterizations of wave-induced temperature fluctuations following an air parcel are needed. These are given by the intrinsic frequency spectra (4) and (5) for the B96-based and MG95 parameterizations, respectively. Again, the two parameterizations give very different results. For temperatures, quasi-invariant spectra $\sim\omega^{-2}$ arise in the B96-based model (4), whereas the MG95-based spectrum (5) follows the shape of the horizontal wavenumber spectrum according to $F_T(\omega/\mathcal{U})$, and its intensity scales with background wind speed $\mathcal{U}$. Analogous differences exist between the heating–cooling rate spectra (11) and (12).

To assess the effects of each parameterization on Lagrangian microphysical models, it is first necessary to generate parcel-based temperature perturbation time series governed by these spectral models. A straightforward approach for the B96-based parameterization is to generate a random time series of the form

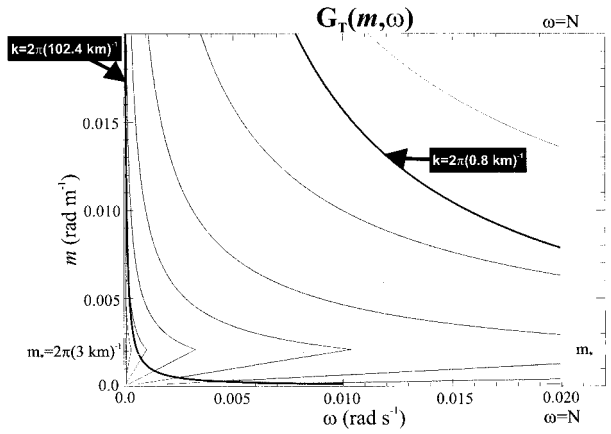

FIG. 3. Model power spectral density of temperature as a function of vertical wavenumber m and intrinsic frequency ω, $G_T(m, \omega)$, from (2) based on the separable model (1) of Gardner et al. (1993a). Contours of this two-dimensional PSD for $m_* = 2\pi\,(3.0\text{ km})^{-1}$ are shown with solid curves. Cusps in the contours at $m = m_*$ mark the shape change in $\hat{A}_\omega(m)$ in (1). For $\omega > N = 0.02$ rad s^{-1} and $\omega < |f| = 10^{-4}$ rad s^{-1}, $G_T(m, \omega)$ is identically zero. Shaded region shows portions of the (m, ω) plane enclosed by curves of constant horizontal wavenumber corresponding to the range of horizontal scales between 102.4 and 0.8 km. For $m_* = 2\pi\,(3.0\text{ km})^{-1}$ approximately 21% of total variance lies within this shaded region.

$$T'_{B96}(t) = \sqrt{2}T_0 \sum_{i=1}^{n} (\hat{B}_T^{B96}(\omega_i)\Delta\omega)^{1/2} \sin(\omega_i t + \phi_i), \quad (13)$$

where $\sqrt{2}$ transforms from rms to peak amplitudes, $\Delta\omega$ is a (constant) frequency step, ω_i is the ith (evenly spaced) frequency, and ϕ_i is a random phase for this harmonic. The frequency step $\Delta\omega$ must be small enough to resolve shape transitions in $B_T^{B96}(\omega)$ adequately, and n and $\Delta\omega$ are chosen so as to integrate $\hat{B}_T^{B96}(\omega_i)$ over its full range between f and N (i.e., $\omega_1 = f + \Delta\omega/2$, $\omega_n = N - \Delta\omega/2$). While this is similar to the Monte Carlo method of Eckermann (1990), many other randomly phased Fourier and/or wavelet synthesis methods could also be used (e.g., Owens 1978; Benzi et al. 1993; Alexander 1996; Elliott et al. 1997). Note that (13) yields Gaussian temperature PDFs and so is also consistent with the PDF-based modeling strategy of Tabazadeh et al. (1996).

The main remaining task is to choose a representative total rms temperature amplitude T_0 for insertion into (13). Here, we attempt a data-based estimate of it from our temperature PSD in Fig. 1b, which was computed over a limited wavenumber range $k_1 < k < k_2$, where $k_1 = 2\pi\,(102.4\text{ km})^{-1}$ and $k_2 = 2\pi\,(0.8\text{ km})^{-1}$. Thus, integrating this spectrum gives us some fraction, ϵ, of T_0^2. We estimate ϵ by numerically integrating $G_T(m, \omega)$ in (2) over all m and ω and comparing it with a second integral constrained within the range $k_1 < k < k_2$. Figure 3 shows a sample contour plot of $G_T(m, \omega)$ for $m_* = 2\pi\,(3\text{ km})^{-1}$. The shaded region shows the integration range on restriction to the horizontal wavenumber range $k_1 < k < k_2$. Using a typical stratospheric value of $m_* = 2\pi\,(3\text{ km})^{-1}$ (Tsuda et al. 1991), we obtain $\epsilon = 0.21$ using representative midlatitude f and N values. Thus, according to the continuous phase-speed model (2), a little over one-fifth of the total variance T_0^2 is contained in the horizontal wavenumber PSDs shown in Fig. 1b and B96.

On numerically integrating the 1D temperature PSD in Fig. 1b, we obtain a variance of 0.16 K^2, and thus a total variance $T_0^2 = 0.16/\epsilon \approx 0.8$ K^2. This is a small value compared to other measurements and analyses (e.g., Tsuda et al. 1991; Allen and Vincent 1995), but it should be kept in mind that a significant fraction of the total ER-2 flight miles during these experiments occurred over open ocean, where wave variances are smaller than those over land (e.g., Nastrom et al. 1987). Furthermore, the mean spectra in Fig. 1b and B96 are log averages of wavelet spectra taken during 1024-s flight intervals. Log averages de-emphasize periods of high activity, and thus the variance of the log-average spectrum is less than the mean variance of the data. Nevertheless, our estimate of $T_0^2 \approx 1$ K^2 can be considered broadly representative of ''ambient'' stratospheric conditions, or a ''lower bound'' estimate. In any given situation, T_0^2 may be considerably larger and may depend on environmental factors such as underlying cloudiness and terrain, background winds (at all levels), altitude, and so on. A sample parcel-based temperature fluctuation time series using $T_0^2 = 0.76$ K^2 in (13) is shown in Fig. 4a.

Temperature perturbation time series for the MG95 parameterization can also be generated by replacing $\hat{B}_T^{B96}(\omega_i)$ in (13) with the corresponding normalized MG95 spectrum $\mathcal{U}^{-1}\hat{F}_T(\omega_i/\mathcal{U})$ from (5). Figure 4b shows the resulting time series, using the same n, T_0, and ϕ_i values as in Fig. 4a, $\mathcal{U} = 50$ m s^{-1}, and where the shape and wavenumber range of the temperature PSD in Fig. 1b was used to specify $\hat{F}_T(\omega_i/\mathcal{U})$. Note the smaller time range and the ''rougher'' appearance of this time series, due to higher-frequency content and a different spectral shape. This time series also highlights a serious shortcoming of the MG95 parameterization: that the gravity wave frequency limits $|f| < |\omega| < N$ are not imposed in this parameterization, and thus unphysical high-frequency temperature oscillations are simulated within air parcels when $\mathcal{U}$ is large.

An additional general caveat must be made about the use of (13) to generate parcel-based temperature fluctuations. For multiparcel trajectory models, we would expect some degree of spatial correlation between the temperature perturbations within closely adjacent parcels. A straightforward application of (13) within such models will not provide these correlations. However, (13) can be generalized to provide spatiotemporal parcel-based temperature fluctuation fields $T'(x, y, z, t)$ using the complete four-dimensional model power spectrum $H_T(k, l, m, \omega)$, assuming isotropy or some other simple directional dependence in wave propagation directions (e.g., Gardner et al. 1993a,b).

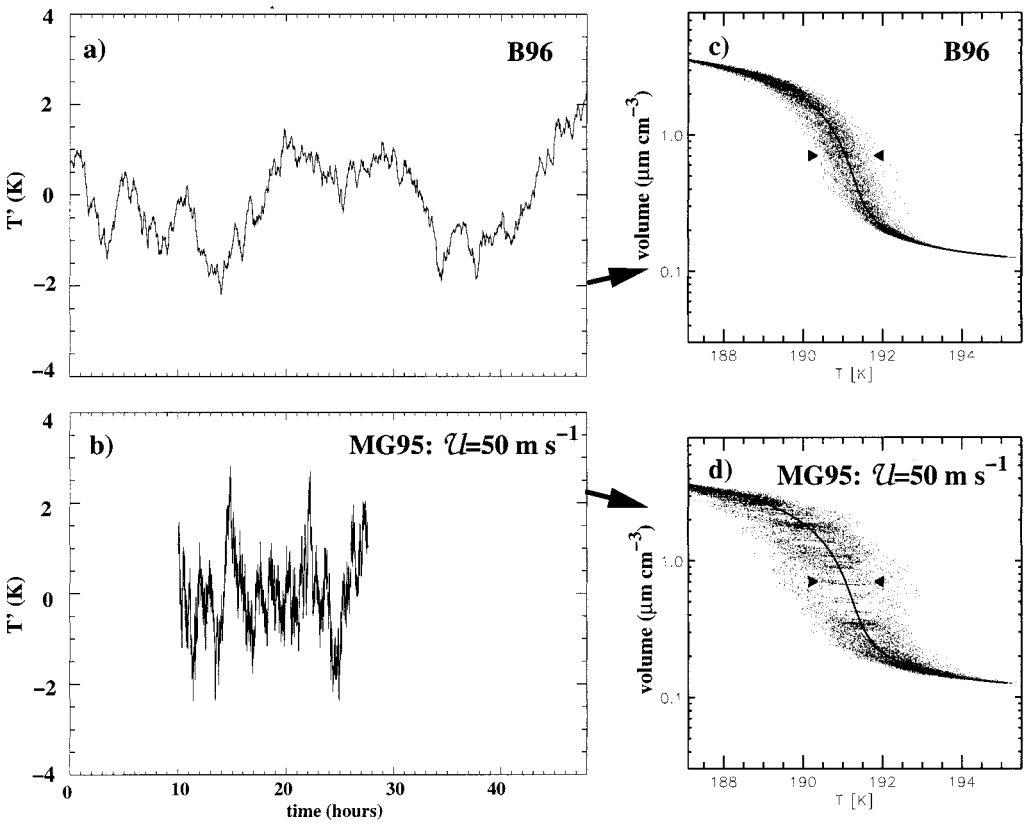

FIG. 4. (a) Temperature as a function of time for an air parcel advected through a random field of gravity waves with an intrinsic frequency spectrum $B(\omega) \sim \omega^{-2}$ between f and N (B96-based approach). (b) Temperature history for an air parcel traversing a stationary wave field with a temperature power spectrum like that in Fig. 1b (MG95 approach). A relative speed of 50 m s^{-1} is assumed for the air parcel with respect to wave field. A total temperature variance $T_0^2 \approx 0.76$ K^2 was used in both cases. Total aerosol volume as a function of temperature for the two different parameterizations of gravity wave temperature fluctuations [(a) and (b)] are shown in (c) and (d), respectively. Aerosol volumes were calculated for ternary $HNO_3/H_2SO_4/H_2O$ droplets using the box model of Meilinger et al. (1995). Each of the aerosol volume plots in (c) and (d) combines the results of four calculations using the temperature perturbation histories in (a) and (b), with different mean temperatures of 188, 190, 191.5, and 193 K. The thin black line in each panel is the thermodynamic equilibrium result for ternary droplets (Carslaw et al. 1994). Arrows depict the approximate range of scatter in the data of Dye et al. (1992).

5. Microphysical effects of the parameterizations

Figures 4a,b show that the B96-based and MG95 parameterizations lead to noticeable differences in simulated mesoscale temperature variability along an air parcel trajectory. Meilinger et al. (1995) and Tsias et al. (1997) have shown that rapid temperature fluctuations can cause the composition of liquid stratospheric aerosols to depart from equilibrium. The extent of nonequilibrium depends upon the cooling or heating rates of air parcels (Tsias et al. 1997), with more rapid cooling or heating leading to greater departures from equilibrium. Under conditions where the stratospheric aerosol is composed principally of H_2SO_4 and H_2O (typically at temperatures $T >$ 195–200 K), the effect of temperature fluctuations can largely be ignored since equilibrium between gas phase H_2O and the droplets is rapidly achieved. The greatest departures from equilibrium occur under conditions where HNO_3 is strongly partitioned from the gas phase into the liquid aerosol, which is typically at $T <$ 195–200 K (Carslaw et al. 1997).

Here, we investigate how each parameterization affects the evolution of ternary $H_2O/HNO_3/H_2SO_4$ aerosol droplets by inserting the time series in Fig. 4a,b into the nonequilibrium microphysical box-trajectory model of Meilinger et al. (1995). We also investigate the effect of these temperature fluctuations on the growth and evaporation of nitric acid trihydrate (NAT) particles. Our aim is to examine how the different natural background temperature fluctuations might affect the instantaneous volumes of these typical stratospheric particles.

In the experiments using this model, parcels were advected along the $\overline{\Theta} = 454$ K isentrope using an initial water vapor mixing ratio of 5 ppmv and an initial gas-phase HNO_3 mixing ratio of 10 ppbv. The perturbation time series in Figs. 4a,b were superimposed upon the

mean temperature, and four separate experiments were conducted for each time series using $\overline{T}$ = 188, 190, 191.5, and 193 K (with corresponding mean pressures $\overline{p}$ = 47, 48.7, 50, and 51.4 hPa, respectively[2]). Total aerosol volume and temperature within the parcel were calculated and recorded at each time step. Results for all four experiments using the B96-based and MG95-based temperature perturbation time series are collated and plotted in Figs. 4c and 4d, respectively. The thin black line on both panels represents the thermodynamical equilibrium curve of Carslaw et al. (1994). Also indicated on each figure is the approximate amount of scatter in observed aerosol volumes (in terms of the equivalent scatter in temperature) measured by Dye et al. (1992) on 24 January 1989. These observations were used by Carslaw et al. (1994), Tabazadeh et al. (1994), and Drdla et al. (1994) for comparison with volumes calculated using a liquid aerosol model assuming thermodynamic equilibrium.

Figures 4c and 4d show that the temperature fluctuations in both the B96-based and MG95 parameterization lead to significant scatter in aerosol volume around the thermodynamic equilibrium value. This is because the time constant for diffusive growth and shrinking of the droplets by HNO_3 mass transfer is rather large compared to the rate of change of air parcel temperature that induces the size changes [for a discussion of these time constants, see Meilinger et al. (1995)]. In particular, it is the large droplets whose growth is diffusively hindered, while, as pointed out by Meilinger et al. (1995) and Tsias et al. (1997), the small droplets adjust their mass rapidly to changes in temperature. However, these small droplets do not contribute significantly to the total aerosol mass. For both the B96-based and MG95 gravity wave parameterizations, the departures in aerosol volume from equilibrium are even greater than those produced by rapid synoptic-scale cooling (Carslaw et al. 1997).

The results using the MG95 parameterization (Fig. 4d) show a great deal more scatter about the equilibrium line in the 189–193 K range than the B96-based results in Fig. 4c. Since there is more rapid heating and cooling of parcels in the MG95 parameterization (see Figs. 4a, b), large aerosol droplets can be rapidly heated to high temperatures before they can adjust by evaporating mass, leading to larger departures from the equilibrium curve. Aerosol volumes a factor of 5–10 larger than equilibrium predictions occur in Fig. 4d. Nonequilibrium behavior is also evident in the B96-based experiments (Fig. 4c) but is much less pronounced, with aerosol volumes generally less than a factor of 2 greater than equilibrium predictions. The strong nonequilibrium behavior in the MG95 parameterization also produces a higher total mean aerosol volume than in the B96-based parameterization.

Clearly the amount of scatter in the B96 case is much closer to that observed by Dye et al. (1992) than is the case for the MG95 trajectory. This may reflect the fact that the MG95 trajectory yields unrealistically rapid cooling and heating rates, and therefore unrealistically broad scatter of calculated aerosol volumes. The calculated scatter in liquid aerosol volumes in the B96 case indicates the ''natural'' range of scatter along an individual trajectory arising from a background of mesoscale temperature fluctuations. The scatter observed by Dye et al. (1992) most likely includes this effect but also contains scatter arising from airmass variations, as well as from instrument noise, particularly at low volumes. Another source of scatter in the measurements is that due to different particle types (most likely in different air masses). The Dye et al. observations from 24 January 1989 appear to be consistent with pure liquid ternary aerosols at all temperatures, which is not the case for observations on other days. Note that the calculated scatter shown here is apparent only where aerosol volumes increase sharply with decreasing temperature, while scatter is apparent at all temperatures in the Dye et al. data. From their measurements alone, it is not possible to say how much of the observed scatter in aerosol volumes was produced by mesoscale temperature fluctuations. However, the observed scatter in the data should represent an upper limit on estimates of the true value of scatter due to temperature fluctuations.

We now consider the effect of the B96-based temperature fluctuations on NAT growth (Fig. 5) using an extended version of the Meilinger et al. (1995) model (Tsias et al. 1997). We show a case where 1% of the background liquid aerosols are assumed to be nucleated as NAT (corresponding to about 0.1 cm^{-3}). NAT particles were assumed to form and evaporate at the NAT equilibrium temperature. It is likely that NAT formation may require a large degree of supercooling or may even occur heterogeneously on ice at temperatures several kelvins lower. The calculated scatter shown here is therefore a lower limit to that expected in reality. Figure 5 shows the scatter in total aerosol volume and is therefore comparable with aerosol volume measurements. The effect of liquid aerosols is relatively minor, so the volumes shown are also rather similar to those of NAT alone. The amount of scatter is now considerably greater than was the case for liquid aerosol growth. The reason is that, with only 0.1 NAT particles cm^{-3}, the individual particles grow rather large and are therefore more strongly diffusively limited than the many smaller liquid aerosols. The amount of scatter is the same as the amplitude of the temperature fluctuations themselves. With 100% NAT activation, the scatter again resembles that for liquid aerosols, while for even fewer NAT particles

[2] Note that Carslaw et al. (1994) used a constant pressure of 55 hPa in calculating aerosol volumes as a function of temperature, implying a change in potential temperature between the different temperatures. Here, the calculations refer to aerosol volumes on a constant potential temperature level. The difference in volume is small.

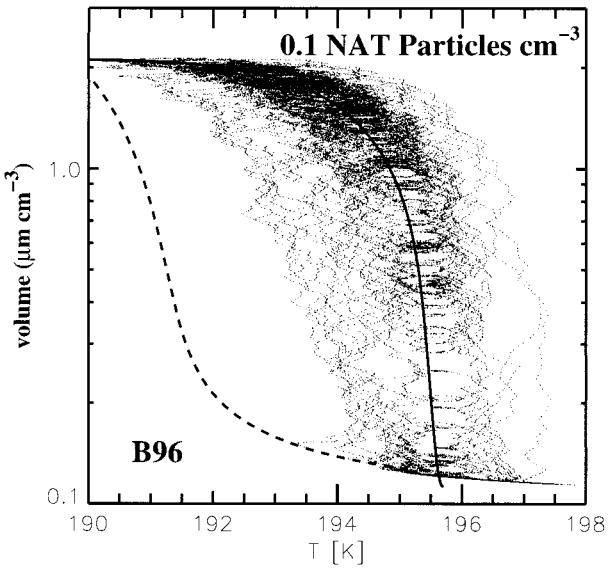

FIG. 5. Total aerosol volume as a function of temperature for NAT particles, where 1% of the background liquid aerosols is assumed to be nucleated as NAT. Results were derived using the parcel-based temperature time series in Fig. 4a (B96), using four different mean temperatures of 188, 190, 191.5, and 193 K. Solid line is NAT volume at equilibrium; dashed line is liquid $HNO_3/H_2SO_4/H_2O$ droplet volume at equilibrium.

it is somewhat greater. For the MG95 temperature fluctuations and 1% NAT, the amount of scatter is somewhat larger than that obtained with the B96-based time series, although the difference is not as pronounced as it was for the liquid aerosols. As the number density of NAT particles increases, the difference in scatter between B96 and MG95 NAT aerosol volumes also increases.

These calculations indicate that, even under ''passive'' background synoptic conditions, a large amount of scatter in aerosol volume can occur due to mesoscale temperature perturbations. Although we have compared the calculated scatter with a single set of in situ particle volume observations, we believe such a natural scatter will be present in all such particle ensembles. This sets a natural limit on the ''quality'' of particle volume and composition measurements. Under some conditions this may make identification of NAT and liquid aerosols in the stratosphere from volume observations alone very difficult unless nonequilibrium growth is taken into account.

6. Summary and discussion

The work of MG95 indicated that the temperature perturbations produced by a spectrum of stratospheric gravity waves had important effects on stratospheric microphysics. Here, we presented revised models of the PSDs of mesoscale temperature and heating and cooling rate perturbations due to such waves, based on the spectral data of B96. The shapes of these PSDs were significantly different from those obtained by MG95. We derived a heating–cooling rate PSD that is more steeply decreasing at the smallest horizontal scales and is far less sensitive to variations in background wind speed (Fig. 1a). Overall, rms heating–cooling rates using the B96-based model were significantly smaller than those derived by MG95.

We developed a simple method for generating random time series of temperature perturbations within air parcels, as governed by either the MG95 or B96-based spectral parameterization. These time series were imported into a microphysical box model to assess the microphysical consequences of each parameterization. Both parameterizations generated total aerosol volumes as a function of air parcel temperature that departed significantly from equilibrium (Figs. 4c,d). The MG95 parameterization generated aerosol volumes that exceeded equilibrium values by up to a factor of 10. The B96-based approach yielded smaller departures, with aerosol volumes generally within a factor of 2 of equilibrium predictions.

The ER-2 aerosol volume versus temperature data of Dye et al. (1992) show significant scatter about the equilibrium curve. In flights for which airmass variations were estimated to be small, aerosol volume as a function of temperature does not appear to show the large departures from equilibrium predicted by the MG95 approach (Fig. 4d). As discussed in section 4, the total temperature variance of $T_0^2 = 0.76$ K^2 used in Fig. 4 is probably a lower bound, and use of a larger T_0^2 in Fig. 4 would yield even greater departures from equilibrium using the MG95 parameterization. Thus, the degree of scatter in the aerosol volume data of Dye et al. (1992) is more closely approximated by a microphysical model using a B96-based parameterization of typical stratospheric mesoscale temperature variability (Fig. 4c).

The differences between the MG95 and B96-based approaches to parameterizing adiabatic gravity wave heating and cooling perturbations arise from the frequency spectrum assumed for the gravity waves in each approach. MG95 assumed (implicitly) a wave field composed entirely of stationary waves, which yields a single intrinsic phase speed that is of similar magnitude to the background stratospheric wind. The B96-based approach assumes that a broad distribution of intrinsic wave phase speeds is present, with a peak centered $\sim$10 m s^{-1} in the lower stratosphere. Thus, waves in B96 are assumed to ''run with'' the background flow to a large degree, reducing the relative speed of air parcels with respect to the waves in regions where background winds are large (e.g., near the edge of the polar vortex).

The full implications of these differences for stratospheric microphysics are not yet clear. Generally speaking, however, both instantaneous and time-averaged aerosol volumes and surface areas will be larger using the MG95 parameterization. However, the duration of cold temperature events due to gravity waves are longer using the B96-based parameterization. This extended residence time in cold conditions could, for example,

lead to increased settling of particles. The time evolution of heterogeneous reactions with strong temperature dependences could also depend on the shape of the frequency spectrum assumed for wave-induced temperature fluctuations. More work is needed to assess these possibilities fully.

We consider it unlikely that the background temperature fluctuations described here could induce nucleation of recognized nitric acid hydrates. The work of Tsias et al. (1997) shows that large-amplitude (>6 K peak to peak) rapid cooling and warming events, such as found in localized mountain-induced gravity waves, would be necessary. In such events, the composition of $HNO_3/H_2SO_4/H_2O$ droplets can approach almost binary HNO_3/H_2O with HNO_3 concentrations in the liquid as high as 59% (by weight), leading to the possible nucleation of nitric acid dihydrate from the droplets. Temperature fluctuations as large and rapid as these are not found in the gravity wave temperature time series considered here (see Fig. 4a). Therefore, hydrate nucleation in temperature fluctuations may well be restricted to regions of the stratosphere directly affected by large-amplitude mountain waves [see, e.g., Fig. 2 of Carslaw et al. (1998b)]. Note, however, that these arguments refer only to homogeneous freezing of nitric acid hydrates from the liquid. As shown by Tabazadeh et al. (1996), background gravity wave temperature fluctuations may sometimes be sufficient to push air parcel temperatures sufficiently below the ice frost point to cause ice nucleation. However, the magnitude of the associated heating–cooling rate fluctuations (D_tT') probably has little influence on this mechanism.

From a purely physical viewpoint, we believe that the B96-based parameterization will be more realistic than the MG95 approach in most circumstances. In passive environments away from strong wave sources, gravity wave spectra have characteristic shapes. While the processes responsible for generating these spectral shapes are still being debated (e.g., Hines 1991; Gardner 1996; Dewan 1997), canonical spectral models that are constrained by the gravity wave dispersion relation, like (1), do a good job in interrelating a wide range of observed gravity wave spectra. In particular, B96 showed that the shapes and intensities of stratospheric horizontal wavenumber spectra measured by aircraft were well predicted by these models. The B96-based parameterization presented here is an extension of these same models to temperature and heating–cooling rate spectra. However, if spectral models other than (1) are preferred, corresponding temperature and heating–cooling rate PSDs can be easily derived from them using similar derivations to those in section 2. The MG95 parameterization, on the other hand, is not constrained by the gravity wave dispersion relation and can generate unphysical high-frequency ($\omega > N$) temperature fluctuations within parcels advected by strong winds.

In regions close to strong wave sources, it is likely that neither spectrally based approach will be the best way to estimate wave temperature perturbations. Alternative models of direct wave propagation from orographic or convective source regions show more promise in this regard (e.g., Bacmeister et al. 1994, 1997b; Alexander 1996; Leutbecher and Volkert 1996) and have started to be incorporated into regional microphysical models (Carslaw et al. 1998a,b; 1999). A complete parameterization of gravity wave effects for chemical and microphysical models may require both a spectral approach, to capture the small-amplitude relatively ubiquitous background wave field, and explicit event-by-event modeling, to capture the rarer large-amplitude wave events generated by strong underlying sources.

Acknowledgments. This research was supported in part by Contracts W-18,566 and L68786D of NASA's Atmospheric Chemistry Modeling and Analysis Program, and contract NAS5-97247 of NASA's Atmospheric Effects of Aviation/Subsonic Assessment Program.

REFERENCES

Alexander, M. J., 1996: A simulated spectrum of convectively generated gravity waves: Propagation from the tropopause to the mesopause and effects on the middle atmosphere. *J. Geophys. Res.,* **101,** 1571–1588.

——, and L. Pfister, 1995: Gravity wave momentum flux in the lower stratosphere over convection. *Geophys. Res. Lett.,* **22,** 2029–2032.

Allen, S. J., and R. A. Vincent, 1995: Gravity-wave activity in the lower atmosphere: Seasonal and latitudinal variations. *J. Geophys. Res.,* **100,** 1327–1350.

Bacmeister, J. T., M. R. Schoeberl, L. R. Lait, P. A. Newman, and B. Gary, 1990: ER-2 mountain wave encounter over Antarctica: Evidence for blocking. *Geophys. Res. Lett.,* **17,** 81–84.

——, S. D. Eckermann, P. A. Newman, L. Lait, K. R. Chan, M. Loewenstein, M. H. Proffitt, and B. L. Gary, 1996: Stratospheric horizontal wavenumber spectra of winds, potential temperature and atmospheric tracers observed by high-altitude aircraft. *J. Geophys. Res.,* **101,** 9441–9470.

——, ——, L. Sparling, K. R. Chan, M. Loewenstein, and M. H. Proffitt, 1997a: Analysis of intermittency in aircraft measurements of velocity, temperature and atmospheric tracers using wavelet transforms. *Gravity Wave Processes and their Parameterization in Global Climate Models,* K. P. Hamilton, Ed., NATO ASI Series, Vol. I50, 85–102.

——, ——, and C. J. Marks, 1997b: Analysis and modeling of stratospheric gravity wave activity along ER-2 flight tracks. The proceedings of the first SPARC general assembly. WMO World Climate Research Rep. 99, Vol. I, 283–286.

Benzi, R. L., A. Biferale, A. Crisanti, G. Paladin, M. Vergassola, and A. Vulpani, 1993: A random process for the construction of multiaffine fields. *Physica D,* **65,** 352–358.

Borrmann, S., S. Solomon, J. E. Dye, D. Baumgardner, K. K. Kelly, and K. R. Chan, 1997: Heterogeneous reactions on stratospheric background aerosols, volcanic sulfuric acid droplets, and type I polar stratospheric clouds: Effects of temperature fluctuations and differences in particle phase. *J. Geophys. Res.,* **102,** 3639–3648.

Cariolle, D., S. Muller, F. Cayla, and M. P. McCormick, 1989: Mountain waves, polar stratospheric clouds, and the ozone depletion over Antarctica. *J. Geophys. Res.,* **94,** 11 233–11 240.

Carslaw, K. S., B. P. Luo, S. L. Clegg, T. Peter, P. Brimblecombe, and P. J. Crutzen, 1994: Stratospheric aerosol growth and HNO_3 gas phase depletion from coupled HNO_3 and water uptake by liquid particles. *Geophys. Res. Lett.,* **21,** 2479–2482.

——, T. Peter, and S. L. Clegg, 1997: Modeling the composition of liquid stratospheric aerosols. *Rev. Geophys.,* **35,** 125–154.
——, and Coauthors, 1998a: Particle microphysics and chemistry in remotely observed mountain polar stratospheric clouds. *J. Geophys. Res.,* **103,** 5785–5796.
——, and Coauthors, 1998b: Increased stratospheric ozone depletion due to mountain-induced atmospheric waves. *Nature,* **391,** 675–678.
——, T. Peter, J. T. Bacmeister, and S. D. Eckermann, 1999: Widespread solid particle formation by mountain waves in the Arctic stratosphere. *J. Geophys. Res.,* **104,** 1827–1836.
Deshler, T., T. Peter, R. Müller, and P. Crutzen, 1994: The lifetime of leewave-induced ice particles in the Arctic stratosphere. I: Balloonborne observations. *Geophys. Res. Lett.,* **21,** 1327–1330.
Dewan, E. M., 1997: Saturated-cascade similitude theory of gravity wave spectra. *J. Geophys. Res.,* **102,** 29 799–29 817.
Drdla, K., and R. P. Turco, 1991: Denitrification through PSC formation: A 1D model incorporating temperature oscillations. *J. Atmos. Chem.,* **12,** 319–366.
——, A. Tabazadeh, R. P. Turco, M. Z. Jacobson, J. E. Dye, C. Twohy, and D. Baumgardner, 1994: Analysis of the physical state of one Arctic polar stratospheric cloud based on observations. *Geophys. Res. Lett.,* **21,** 2475–2478.
Dye, J. E., and Coauthors, 1992: Particle size distributions in Arctic polar stratospheric clouds, growth and freezing of sulfuric acid droplets, and implications for cloud formation. *J. Geophys. Res.,* **97,** 8015–8034.
Eckermann, S. D., 1990: Effects of nonstationarity on spectral analysis of mesoscale motions in the atmosphere. *J. Geophys. Res.,* **95,** 16 685–16 703.
——, 1995: Effect of background winds on the vertical wavenumber spectrum of atmospheric gravity waves. *J. Geophys. Res.,* **100,** 14 097–14 112.
——, D. E. Gibson-Wilde, and J. T. Bacmeister, 1998: Gravity wave perturbations of minor constituents: A parcel advection methodology. *J. Atmos. Sci.,* **55,** 3521–3539.
Elliott, F. W., Jr., D. J. Horntrop, and A. J. Majda, 1997: A Fourier-wavelet Monte Carlo method for fractal random fields. *J. Comput. Phys.,* **132,** 384–408.
Fritts, D. C., and T. E. VanZandt, 1993: Spectral estimates of gravity wave energy and momentum fluxes. Part I: Energy dissipation, acceleration, and constraints. *J. Atmos. Sci.,* **50,** 3685–3694.
Fromm, M. D., J. D. Lumpe, R. M. Bevilacqua, E. P. Shettle, J. Hornstein, S. T. Massie, and K. H. Fricke, 1997: Observations of Antarctic polar stratospheric clouds by POAM II: 1994–1996. *J. Geophys. Res.,* **102,** 23 659–23 672.
Gardner, C. S., 1996: Testing theories of atmospheric gravity wave saturation and dissipation. *J. Atmos. Terr. Phys.,* **58,** 1575–1589.
——, C. A. Hostetler, and S. J. Franke, 1993a: Gravity wave models for the horizontal wave number spectra of atmospheric velocity and density perturbations. *J. Geophys. Res.,* **98,** 1035–1049.
——, ——, and S. Lintelman, 1993b: Influence of the mean wind field on the separability of atmospheric perturbation spectra. *J. Geophys. Res.,* **98,** 8859–8872.
Godin, S., G. Mégie, C. David, D. Haner, C. Flesia, and Y. Emery, 1994: Airborne lidar observation of mountain-wave-induced polar stratospheric clouds during EASOE. *Geophys. Res. Lett.,* **21,** 1335–1338.
Hines, C. O., 1991: The saturation of gravity waves in the middle atmosphere. Part II: Development of Doppler-spread theory. *J. Atmos. Sci.,* **48,** 1360–1379.
Jensen, E. J., and G. E. Thomas, 1994: Numerical simulations of the effects of gravity waves on noctilucent clouds. *J. Geophys. Res.,* **99,** 3421–3430.
——, and O. B. Toon, 1994: Ice nucleation in the upper troposphere: Sensitivity to aerosol number density, temperature and cooling rate. *Geophys. Res. Lett.,* **21,** 2019–2022.
——, ——, L. Pfister, and H. B. Selkirk, 1996: Dehydration of the upper troposphere and lower stratosphere by subvisible cirrus clouds near the tropical tropopause. *Geophys. Res. Lett.,* **23,** 825–828.
Koop, T., U. M. Biermann, W. Raber, B. P. Luo, P. J. Crutzen, and T. Peter, 1995: Do stratospheric aerosol droplets freeze above the ice frost point? *Geophys. Res. Lett.,* **22,** 917–920.
——, B. P. Luo, U. M. Biermann, P. J. Crutzen, and T. Peter, 1997: Freezing of $HNO_3/H_2SO_4/H_2O$ solutions at stratospheric temperatures: Nucleation statistics and experiments. *J. Phys. Chem.,* **101,** 1117–1133.
Leutbecher, M., and H. Volkert, 1996: Stratospheric temperature anomalies and mountain waves: A three-dimensional simulation using a multiscale weather prediction model. *Geophys. Res. Lett.,* **23,** 3329–3332.
Lin, H., K. J. Noone, J. Ström, and A. J. Heymsfield, 1998: Dynamical influences on cirrus cloud formation process. *J. Atmos. Sci.,* **55,** 1940–1949.
Meilinger, S. K., T. Koop, B. P. Luo, T. Huthwelker, K. S. Carslaw, U. Krieger, P. J. Crutzen, and T. Peter, 1995: Size-dependent stratospheric droplet composition in lee wave temperature fluctuations and their potential role in PSC freezing. *Geophys. Res. Lett.,* **22,** 3031–3034.
Murphy, D. M., and B. L. Gary, 1995: Mesoscale temperature fluctuations and polar stratospheric clouds. *J. Atmos. Sci.,* **52,** 1753–1760.
Nastrom, G. D., and K. S. Gage, 1985: A climatology of atmospheric wavenumber spectra of wind and temperature observed by commercial aircraft. *J. Atmos. Sci.,* **42,** 950–960.
——, D. C. Fritts, and K. S. Gage, 1987: An investigation of terrain effects on the mesoscale spectrum of atmospheric motions. *J. Atmos. Sci.,* **44,** 3087–3096.
Owens, A. J., 1978: An algorithm for generating fluctuations having an arbitrary power spectrum. *J. Geophys. Res.,* **83,** 1673–1675.
Peter, T., R. Müller, P. J. Crutzen, and T. Deshler, 1994: The lifetime of leewave-induced ice particles in the Arctic stratosphere. II: Stabilization due to NAT-coating. *Geophys. Res. Lett.,* **21,** 1331–1334.
Potter, B. E., and J. R. Holton, 1995: The role of monsoon convection in the dehydration of the lower tropical stratosphere. *J. Atmos. Sci.,* **52,** 1034–1050.
Tabazadeh, A., R. P. Turco, K. Drdla, M. Z. Jacobson, and O. B. Toon, 1994: A study of type I polar stratospheric cloud formation. *Geophys. Res. Lett.,* **21,** 1619–1622.
——, O. B. Toon, B. L. Gary, J. T. Bacmeister, and M. R. Schoeberl, 1996: Observational constraints on the formation of type 1a polar stratospheric clouds. *Geophys. Res. Lett.,* **23,** 2109–2112.
Tsias, A., A. J. Prenni, K. S. Carslaw, T. P. Onasch, B. P. Luo, M. A. Tolbert, and T. Peter, 1997: Freezing of polar stratospheric clouds in orographically induced strong warming events. *Geophys. Res. Lett.,* **24,** 2303–2306.
Tsuda, T., T. E. VanZandt, M. Mizumoto, S. Kato, and S. Fukao, 1991: Spectral analysis of temperature and Brunt–Väisälä frequency fluctuations observed by radiosondes. *J. Geophys. Res.,* **96,** 17 265–17 278.
Turco, R. P., O. B. Toon, R. C. Whitten, R. G. Keesee, and D. Hollenbach, 1982: Noctilucent clouds: Simulation studies of their genesis, properties and global influences. *Planet. Space Sci.,* **30,** 1147–1181.
Vincent, R. A., and S. D. Eckermann, 1990: VHF radar observations of mesoscale motions in the troposphere: Evidence of gravity wave Doppler shifting. *Radio Sci.,* **25,** 1019–1037.
Whiteway, J. A., T. J. Duck, D. P. Donovan, J. C. Bird, S. R. Pal, and A. I. Carswell, 1997: Measurements of gravity wave activity within and around the Arctic stratospheric vortex. *Geophys. Res. Lett.,* **24,** 1387–1390.